

# Self-consistent many-body metrology

Jae-Gyun Baak<sup>1</sup> and Uwe R. Fischer<sup>1</sup>

<sup>1</sup>*Seoul National University, Department of Physics and Astronomy,  
Center for Theoretical Physics, Seoul 08826, Korea*

(Dated: May 2, 2024)

We investigate performing classical and quantum metrology and parameter estimation by using interacting trapped bosons, which we theoretically treat by a self-consistent many-body approach of the multiconfigurational Hartree type. Focusing on a tilted double-well geometry, we compare a self-consistently determined and monitored two-mode truncation, with dynamically changing orbitals, to the conventional two-mode approach of fixed orbitals, where only Fock space coefficients evolve in time. We demonstrate that, as a consequence, various metrological quantities associated to a concrete measurement such as the classical Fisher information and the maximum likelihood estimator are deeply affected by the orbitals' change during the quantum evolution. Self-consistency of the quantum many-body dynamics of interacting trapped ultracold gases thus fundamentally affects the attainable parameter estimation accuracy of a given metrological protocol.

Within the currently emerging quantum era, quantum metrology [1–8] has proven itself to be a powerful tool for the accurate estimation of even very small physical parameters, such as gravitational wave amplitudes [9], or to limit the attainable measurement accuracy of fundamental constants like the speed of light [10]. As a result, quantum metrology promises to revolutionize the existing technologies of measurement.

While quantum metrology has frequently been employed in the quantum optical context [11–14], more recently the corresponding experiments and theory are also exploring coherent matter waves cf., e.g., Refs. [15–30]. Photons freely propagating in the quantum vacuum are to a very good approximation noninteracting particles and are well described by plane waves of definite momentum. Matter waves forming Bose-Einstein condensates at very low temperatures are, however, interacting by the scattering of their elementary atomic or molecular constituents, and are spatially confined (trapped) by arbitrary scalar potentials. In what follows, we show that the full self-consistency of the quantum many-body evolution of such a system needs in general to be taken into account, to yield reliable parameter estimation. We demonstrate that the interplay of Fock space amplitudes and time-dependent field operator modes (:= orbitals), representing self-consistent many-body evolution, is crucial. This interplay is not obtained when fixing the orbitals' shape, thereby significantly restricting the associated Hilbert space.

We take as an archetypical model system and for concreteness a tilted double well, where the parameter to be estimated is the linear slope  $p_4$  which could, e.g., represent exposing the gas to constant gravitational acceleration (see Fig. 1). To facilitate comparison with conventional interferometry, we operate within a (continuously monitored) two-mode approximation (TMA), corresponding to two interferometric arms. We consider a simple (Mach-Zehnder type) experiment which counts the final number of particles on the left and right. It

is demonstrated that while a non-self-consistent evolution yields a null result for  $p_4$  [zero classical Fisher information (CFI)], a self-consistent quantum many-body evolution gives finite CFI, enabling  $p_4$  estimation. We therefore conclusively show that self-consistency is crucial for the correct interpretation of parameter estimation data in a trapped interacting many-body system. We note that Heisenberg-limit number scaling of estimation precision with  $1/N$  [instead of the shot noise (standard quantum) limit  $\propto 1/\sqrt{N}$ ], for cat state distributions in Fock space [28], or an enhanced  $N$ -scaling relying on  $k$ -body interactions [31, 32], are not our aim in the present work. The focus is on the fundamental imprint of the self-consistency of many-body evolution on the accuracy of parameter estimation from the metrological protocol.

To determine the many-body evolution self-consistently, we perform a multiconfigurational time-dependent Hartree (MCTDH) analysis. This

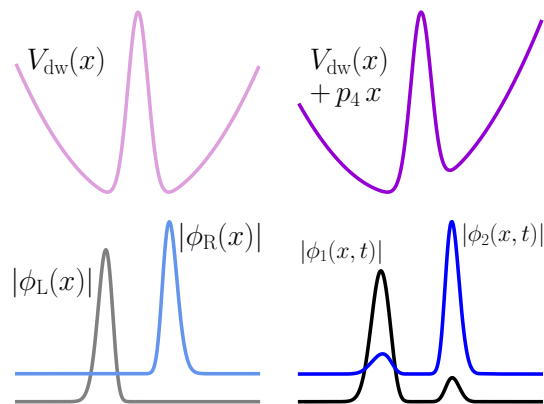


FIG. 1. Top: Trap potential. Left:  $t < 0$ , symmetric double well. Right: At  $t = 0$ , the tilt is switched on. Bottom: Initially localized orbitals in the large-barrier double-well self-consistently evolve in time after tilting, and become delocalized, whereas without self-consistency they remain localized. The orbitals are vertically offset for clarity.

is a well tested method to describe the dynamics of spatially confined quantum systems, such as the one under investigation here, for which self-consistency is crucial [33–37]. The general  $N$ -body state reads

$$|\Psi(t)\rangle = \sum_{\vec{n}} C_{\vec{n}}(t) |\vec{n}(t)\rangle, \quad (1)$$

where  $\sum_{\vec{n}} |C_{\vec{n}}|^2 = 1$  for state normalization and  $\vec{n}$  denotes the set of occupation numbers  $\{n_i | i = 1, 2, \dots, M\}$  in each mode (orbital), with  $\sum_{i=1}^M n_i = N$ . The time-dependent Fock basis state  $|\vec{n}(t)\rangle$  indicates that the orbitals change in time as a result of finite  $M$  (see, Fig. 1). Their dynamics follows the system of nonlinear coupled integrodifferential Eqs. (S1) in the supplement [38]. Numerical solution enables the determination of Fock space coefficients  $C_{\vec{n}}$  and orbitals in a self-consistent manner at any time [39].

The quantum metrological approach to parameter estimation, see for example Refs. [40–44], proceeds essentially as follows. An initial state  $|\psi\rangle$  experiences a dynamical evolution, e.g.,  $e^{-i\hat{H}_X t}$ , during the time  $t$  and the final state  $|\psi_X\rangle$  contains the information of the parameter  $X$ . One chooses an appropriate measurement on  $|\psi_X\rangle$  to estimate  $X$ . Previous studies on quantum metrology with ultracold atoms [15–30, 42] have focused on the coefficients  $C_{\vec{n}}(X; t)$  in Eq. (1), and have calculated the quantum Fisher information (QFI)  $\mathfrak{F}_X$  from  $C_{\vec{n}}(X; t)$  only. However, since the orbitals also evolve by Eqs. (S1) and the time evolution relies on  $X$ , the  $|\vec{n}(X; t)\rangle$  must be considered in the calculation of both the QFI and the CFI. To evaluate the sensitivity of a quantum mechanical state to a parameter change thus requires full exploitation of the information encoded in the state. Here, we make full use of the parameter dependence of the state, reflected in both coefficients and orbitals. As a result, we establish numerically exact many-body parameter estimation for trapped interacting quantum gases.

A scalar bosonic gas with contact interactions, trapped in a quasi-one-dimensional (quasi-1D) double-well potential, is described by the Hamiltonian

$$\hat{H} = \sum_{j=1}^N \left\{ -\frac{1}{2} \frac{\partial^2}{\partial x_j^2} + V(x_j) \right\} + g \sum_{j < k}^N \delta(x_j - x_k), \quad (2)$$

where  $V$  is the trap potential. We render  $\hat{H}$  in a dimensionless form, fixing a unit length  $L$ ; the unit of time is then  $L^2$  for  $\hbar = m = 1$  [45]. The quasi-1D interaction coupling  $g$  is controllable by either Feshbach or geometric scattering resonances [46]. Exact solutions of the Schrödinger equation associated to Eq. (2) exist for homogeneous gases under periodic boundary conditions or in a box trap; their metrology was explored in [47].

We assume a trap potential of the form  $V(x) = V_{\text{dw}}(x) + p_4 x = \frac{1}{2} p_1 x^2 + p_2 \exp[-x^2/(2p_3^2)] + p_4 x$ , where  $p_4 = 0$  initially, cf. Fig. 1. The remaining parameters,

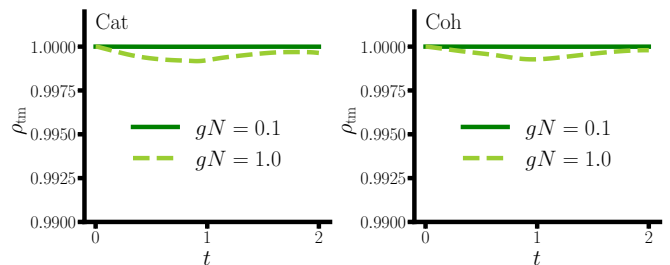


FIG. 2. Monitoring the two-mode truncation after turning on  $p_4$ , verifying whether  $\rho_{\text{tm}} = (\rho_1 + \rho_2)/N \lesssim 1$  (we put  $N = 10$ ), for cat state (left) and spin-coherent state (right).

$p_1 = 0.5$ ,  $p_2 = 50$ , and  $p_3 = 1$ , are fixed throughout the evolution. The two lowest-energy single-particle states are symmetric and antisymmetric with respect to the origin, respectively, and their addition and subtraction results in two well-localized orbitals: left  $\phi_L(x)$  and right  $\phi_R(x)$ , see Fig. 1. These orbitals, approximate ground states of each well, furnish the two modes [48].

The estimation process of  $p_4$  proceeds with an initial state in the form of Eq. (1). With  $\phi_L(x)$  and  $\phi_R(x)$ , we employ two coefficient distributions: A NOON (cat) state,  $|\psi_0\rangle = (|N, 0\rangle + |0, N\rangle)/\sqrt{2}$ , and a spin-coherent state  $|\psi_0\rangle = \sum_{k=0}^N \sqrt{\frac{N!}{k!(N-k)!}} \cos^{N-k}(\frac{\pi}{4}) \sin^k(\frac{\pi}{4}) |N - k, k\rangle$ . Then a small  $p_4$  tilt is switched on. The state then evolves according to Eqs. (S1); finally, the number of particles in each well is measured and  $p_4$  is estimated from the set of outcomes.

As the relative interaction strength  $gN$  (typical ratio of interaction over single-particle energies), increases, more modes than two are required to correctly reproduce the many-body dynamics [37]. Keeping  $gN$  fixed when taking the limit  $N \rightarrow \infty$  has been demonstrated to reproduce the Gross-Pitaevskii ground state energy [49, 50]. We thus keep in the following  $gN$  fixed when varying  $N$ , to remain close to the TMA. In order to adequately compare self-consistent (SC) evolution to conventional SU(2) two-mode interferometry (TMI), which operates with changing Fock space coefficients only, we maintain TMA validity throughout the time evolution. This can be assessed by evaluating  $\rho_{\text{tm}} := (\rho_1 + \rho_2)/N$ , cf. Fig. 2, where  $\rho_j$  is the  $j$ th largest eigenvalue of the reduced one-body density matrix,  $\rho^{(1)}(x, x'; t)$ ; see (S2) in the supplement [38]. After diagonalization,  $\rho^{(1)}(x, x') = \sum_j \rho_j(t) \phi_j^{(\text{no})}(x', t) \phi_j^{(\text{no})}(x, t)$ , with the *natural orbitals*  $\{\phi_j^{(\text{no})}(x, t) | j = 1, 2, \dots\}$ . When a single  $\rho_1 = O(N)$  (in the formal limit  $N \rightarrow \infty$ ), a Bose-Einstein condensate is obtained. For several  $\rho_j$  of  $O(N)$ , we have a fragmented condensate [51]. The validity of the TMA (two-fold fragmented condensate) depends on whether  $\rho_1 \simeq \rho_2 \simeq N/2$  and  $\rho_{\text{tm}} \simeq O(1)$  hold. In the supplement [38], we provide further evidence for the appropriateness of using the TMA, by demonstrating the rapid convergence of our re-

sults with increasing  $M$ .

We define an initial state using four orbitals ( $M = 4$ ), which are including  $\phi_L(x)$  and  $\phi_R(x)$ , and then monitor the natural occupations  $\rho_j$  under self-consistent evolution at nonzero  $p_4$ , for both cat and spin-coherent states. Fig. 2 shows  $\rho_{\text{tm}}$ , where we observe it is close to unity. Also, both  $\rho_1$  and  $\rho_2$  are macroscopically occupied during the evolution, with negligible occupations  $\rho_3$  and  $\rho_4$ . This however also depends on the parameter regime used. When  $gN = 0.1$ , two modes are sufficient, but when  $gN = 1$ ,  $\rho_{\text{tm}}$  discernibly dips below unity. Increasing  $p_4$  further, the TMA fails. An appropriate regime of parameters where  $\rho_{\text{tm}} \simeq 1$  is obtained by fixing  $gN = 0.1$  and  $p_4 = 0.1$ . Also, even though natural orbitals are used in the discussion above, we can apply the two-mode criterion to the left/right orbitals or their time-evolved forms, i.e.,  $\phi_1(x, t)$  and  $\phi_2(x, t)$ ; there always exists a unitary transformation such that  $\phi_j(x, t) = \sum_{jk} U_{jk} \phi_k^{(\text{no})}(x, t)$ .

Expanding the second-quantized form of Eq. (2) with  $\hat{\Psi}(x) = \hat{b}_L \phi_L(x) + \hat{b}_R \phi_R(x)$ , a two-site single-band Bose-Hubbard Hamiltonian is obtained. In terms of the usual SU(2) Pauli matrices  $\hat{J}_x = \frac{1}{2}(\hat{b}_L \hat{b}_R + \hat{b}_R^\dagger \hat{b}_L)$  and  $\hat{J}_z = \frac{1}{2}(\hat{b}_L \hat{b}_L - \hat{b}_R^\dagger \hat{b}_R)$ ,

$$\hat{H} = -\tau \hat{J}_x + \epsilon \hat{J}_z + U \hat{J}_z^2, \quad (3)$$

where  $\tau$  is tunneling amplitude,  $\epsilon$  an energy offset between wells, and  $U \propto g$  an interaction coupling, all depending on integrals involving the two orbitals. The implementation of quantum metrological protocols using the above Hamiltonian was carried out, e.g., in Refs. [19, 24, 44]: An initial state  $|\psi_0\rangle$ , as defined by the distribution of coefficients  $C_{\vec{n}}$ , evolves as  $\exp(-i\hat{H}t)|\psi_0\rangle$ , and the parameter of interest, e.g.,  $\epsilon$ , is estimated from the population imbalance [19, 24]. In our setup, the strong barrier renders the initial  $\tau$  exponentially small compared to  $\epsilon$  and  $U$ , and  $\epsilon \neq 0$ , as the symmetry of  $V(x)$  is broken by  $p_4$ . Hence the TMI time evolution operator is, to very good accuracy,  $\exp(-i(\epsilon \hat{J}_z + U \hat{J}_z^2)t)$ , and the QFI can be analytically calculated by  $\mathfrak{F}_\epsilon = 4 \langle \psi_0 | (\Delta \hat{J}_z)^2 | \psi_0 \rangle$ . When the cat state is used,  $\mathfrak{F}_\epsilon = N^2 t^2$ , which is denoted as the Heisenberg limit. For the spin-coherent state,  $\mathfrak{F}_\epsilon = N \sin^2(\theta) t^2$ , representing the shot-noise (standard quantum) limit. Any nonzero  $\tau$  deteriorates the  $N$ -scaling of  $\mathfrak{F}_\epsilon$ , confirmed by numerically calculating the QFI [19]. Note that here only the change of Fock space coefficients has been considered, while the orbitals are fixed in TMI. Because of the latter fact, the still exponentially small  $\tau$  and  $U$  are kept constant during the evolution, and  $\epsilon$  is abruptly switched on at  $t = 0$ . In our setting,  $\epsilon \in (-0.7, -0.6)$ , and  $U \in (0.002, 0.03)$ , with concrete values determined by  $gN$  and  $N$ , on which in turn the initial orbitals  $\phi_L(x)$  and  $\phi_R(x)$  depend. Recall that our target parameter is  $p_4$ , not  $\epsilon$ , thus by using the chain rule,  $\mathfrak{F}_{p_4} = \mathfrak{F}_\epsilon \times (h_1 - h_2)^2$ , where the single-particle energies  $h_i := \int dx \phi_i^*(x) \left[ -\frac{1}{2} \frac{\partial^2}{\partial x^2} + V(x) \right] \phi_i(x)$ .

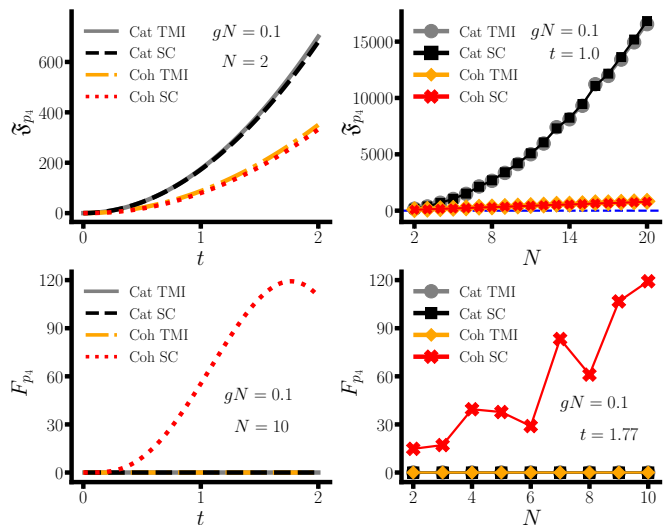


FIG. 3. First and second row display quantum ( $\mathfrak{F}$ ) and classical ( $F$ ) Fisher information, respectively, plotted versus time  $t$  (left) and particle number  $N$  (right), for cat and coherent (coh) states, respectively. At the maximum on the lower left plot, which is at  $t = 1.77$ , the tunneling amplitude in the SC evolution has increased to  $\tau \simeq 0.09$  (for  $N = 10$ ).

First, we compare the QFIs of the SC approach and the conventional TMI. The QFI with respect to a given parameter  $X$  inscribed onto a pure state  $|\psi_X\rangle$ , is  $\mathfrak{F}_X = 4(\langle \partial_X \psi_X | \partial_X \psi_X \rangle - |\langle \psi_X | \partial_X \psi_X \rangle|^2)$ , and insertion of Eq. (1) into  $|\psi_X\rangle$  gives Eq. (S4), which facilitates calculation of the QFI using the ingredients of MCTDH from the expansion in Eq. (1), also cf. [38]. The first row in Fig. 3 shows QFI versus time  $t$  and particle number  $N$ , respectively. For each initial state, the SC method reproduces very well the QFI predicted by TMI. The influence of self-consistency thus plays a subdominant role for  $\mathfrak{F}_X$ . The latter completely depends on the final state, and self-consistency (changing orbitals) essentially represents fitting that state more exactly. When the bosons weakly interact ( $gN = 0.1$ ) and the disturbance to the system is small ( $p_4 = 0.1$ ), conventional TMI therefore approximates well the QFI [52].

We now turn to the CFI [53, 54], associated to a concrete measurement, for which, as we show, the impact of self-consistency becomes manifest. Counting the number of bosons in each well constitutes our measurement, so that the CFI is defined as

$$F_{p_4} = \sum_{\vec{n}} P(\vec{n}|p_4) \left( \frac{\partial \log P(\vec{n}|p_4)}{\partial p_4} \right)^2, \quad (4)$$

where  $P(\vec{n}|p_4)$  is the probability distribution (likelihood)  $\vec{n} = (n_L, n_R)$ , given  $p_4$ , and  $n_L$  and  $n_R$  are the numbers of particles that reside in the left and the right well, respectively. An appropriate  $P(\vec{n}|p_4)$  has to be constructed to calculate the CFI and the conventional TMI approach considers that  $P(\vec{n}|p_4) :=$

$|\langle \vec{n}(t) | \Psi(t) \rangle|^2$ . Then, the CFI *always exactly vanishes*, irrespective of the initial state, as the Hamiltonian contains only  $\hat{J}_z$  and  $\hat{J}_z^2$ . TMI time evolution therefore just changes the phases of the coefficients:  $C_k(t) = \exp(-i\epsilon \frac{N-2k}{2} t) \exp(-iU(\frac{N-2k}{2})^2 t) C_k(0)$ , where the state  $|\psi(t)\rangle = \sum_{k=0}^N C_k(t) |N-k, k\rangle = \exp(-i(\epsilon \hat{J}_z + U \hat{J}_z^2)t) |\psi(0)\rangle$  and  $\hat{J}_z |N-k, k\rangle = \frac{N-2k}{2} |N-k, k\rangle$ . Then  $P(\vec{n} = (N-k, k) | p_4) = |C_k(t)|^2 = |C_k(0)|^2$ , independent of  $p_4$ , yielding vanishing CFI, cf. [38].

On the other hand, when both orbitals and Fock space coefficients evolve in the SC framework, the initial interpretation of the orbitals cannot be maintained throughout the time evolution. Initially well-localized orbitals, i.e.,  $\phi_L(x) = \phi_1(x, 0)$  and  $\phi_R(x) = \phi_2(x, 0)$ , correspond to particles being found in the left and right well, respectively. However, the orbitals change with time during the many-body evolution, so  $\phi_1(x, t)$  and  $\phi_2(x, t)$ , do not necessarily imply left or right localization at the time of measurement. Therefore, simply computing  $P(\vec{n} | p_4) = |\langle \vec{n}(t) | \Psi(t) \rangle|^2$ , as in the TMI approach, is not applicable. In the bosonic field operator  $\hat{\Psi}(x) = \sum_j \hat{b}_j(t) \phi_j(x, t)$ , it is clear that the bosonic annihilation operator  $\hat{b}_j(t)$  corresponds to the time-evolving orbital  $\phi_j(x, t)$ , which delocalizes with increasing  $t$ , see Fig. 1. Thus the Fock state in Eq. (1)  $|\vec{n}(t)\rangle = \frac{(\hat{b}_1^\dagger(t))^{n_1} (\hat{b}_2^\dagger(t))^{n_2} \dots (\hat{b}_M^\dagger(t))^{n_M}}{\sqrt{n_1! n_2! \dots n_M!}} |0\rangle$  cannot by itself project the quantum state into any of  $|\vec{n}\rangle$  and  $\langle \vec{n}(t) | \Psi(t) \rangle$  cannot be interpreted as probability amplitude for each measurement outcome as in TMI. In other words,  $|\vec{n}(t)\rangle$  and  $|\vec{n}\rangle$ , while initially identical, become different due to SC evolution. Hence we need to re-establish a connection between time-evolving orbitals and  $|\vec{n}\rangle$  that corresponds to a measurement outcome, resulting in the proper distribution  $P(\vec{n} | p_4) = |\langle \vec{n} | \Psi(t) \rangle|^2 \neq |\langle \vec{n}(t) | \Psi(t) \rangle|^2$ .

Within SC time evolution after a trap tilt,  $\phi_1(x, t)$  and  $\phi_2(x, t)$  remain well-localized in the case of a cat state. That is,  $\phi_1(x, t)$  ( $\phi_2(x, t)$ ) begins from  $\phi_1(x, 0) = \phi_L(x)$  [ $\phi_2(x, 0) = \phi_R(x)$ ] and their absolute value remains nearly identical except slightly wider (narrower) width and shorter (taller) height, respectively. For the spin-coherent state, however,  $\phi_1(x, t)$  and  $\phi_2(x, t)$  spread into opposite wells while they evolve under nonzero  $p_4$ ; see Fig. 1. Then even when a particle resides in  $\phi_1(x, t)$  or  $\phi_2(x, t)$ , to assign it to the left or right well is ambiguous. One can however still define mathematically “left” or “right” by integrating the orbitals from  $-\infty$  to the center point  $x = 0$  of  $V(x)$  and from the center point of  $V(x)$  to  $\infty$ , respectively:  $P_{\text{Left}} = \int_{-\infty}^0 |\phi_j(x, t)|^2 dx$  and  $P_{\text{Right}} = \int_0^{\infty} |\phi_j(x, t)|^2 dx$ . One can then construct  $P(\vec{n} | p_4)$  by computing the permanent of a special matrix composed from  $P_{\text{Left}}$  and  $P_{\text{Right}}$ . The computable  $N$  range is limited, though, due to rapidly increasing algorithmic complexity when calculating a matrix permanent, see [38].

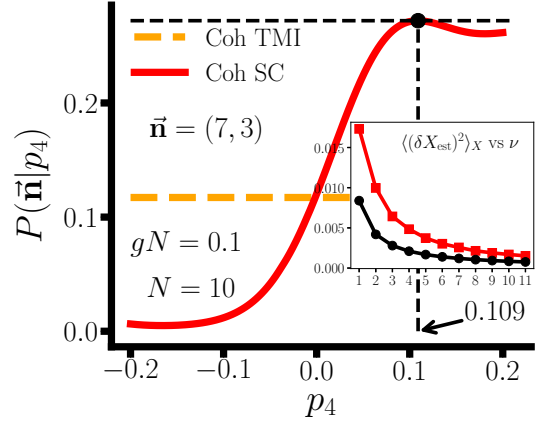


FIG. 4. Single implementation of the MLE for an estimate of  $p_4$  using the spin-coherent state. Red solid line is for the SC approach and orange dashed line (a constant  $\forall p_4$ ) for the TMI. In the inset, red squares represent the mean-square deviation and black rounds the Cramér-Rao lower bound from Eq. (5).

The second row in Fig. 3 shows the CFI versus  $t$  and  $N$ . Fixed orbitals results in vanishing CFI, as expected. Also, even within SC evolution, the cat state shows almost vanishing CFI, which is attributed to the fact that the orbitals stay localized in each well during the whole evolution time and the probabilities, i.e.,  $P_{\text{Left}}$  and  $P_{\text{Right}}$ , remain nearly constant (for small  $p_4$ ). Thus under the given measurement the change of  $P(\vec{n} | p_4)$  with respect to  $p_4$  is negligible. However, the spin-coherent state displays a significant change in orbitals and increasing CFI during the early stage. Bottom right in Fig. 3 shows the  $N$ -scaling of the CFI; the SC approach with spin-coherent state shows an almost linearly increasing CFI. The complex fluctuation pattern appears because of the short time  $t = 1.77$  after a nonzero  $p_4$  is suddenly applied, and for increasing  $t$  these fluctuations smoothen out. Thus a SC approach may yield drastically different metrological predictions from a TMI based method.

Fig. 4 shows our primary result: The implementation of parameter estimation at the final stage of the metrological protocol. The maximum likelihood estimator (MLE) [6, 55] is used as a concrete example, because it asymptotically saturates the Cramér-Rao bound for an infinite number of measurements ( $\nu \rightarrow \infty$ , see also [38])

$$\langle (\delta X_{\text{est}})^2 \rangle_X \geq \frac{1}{\nu F_X}. \quad (5)$$

Here, the parameter  $X$  is our  $p_4$ ,  $X_{\text{est}}$  is an estimator of  $X$ , and  $\delta X_{\text{est}} := X_{\text{est}} / |\partial \langle X_{\text{est}} \rangle_X / \partial X| - X$ , with average  $\langle \dots \rangle_X$  taken with respect to  $P(\vec{n} | p_4)$ .

In Fig. 4, the likelihood function  $P(\vec{n} | p_4)$  is displayed, supposing, for concreteness, that the measurement outcome is  $\vec{n} = (7, 3)$ , where  $n_L$  and  $n_R$  denote number of particles in left and right well, respectively. Red solid line shows the maximum of  $P(\vec{n} | p_4)$  at  $p_4 \simeq 0.109$ , thus

the estimate of  $p_4$ , given  $\bar{\mathbf{n}} = (7, 3)$ , is  $X_{\text{est}} \simeq 0.109$ . Similarly, every single outcome, 11 in total, is connected to an estimate of  $p_4$ . The orange dashed line obtained by conventional TMI with a spin-coherent state stays flat, which means that the information given by the measurement outcome  $\bar{\mathbf{n}} = (7, 3)$  is zero, and an estimate of  $p_4$ , in accordance with  $F_{p_4} = 0$ , is not possible.

When  $\langle X_{\text{est}} \rangle_X = X$  holds, an estimator is unbiased. The present MLE is not unbiased except infinitesimally close to  $p_4 = 0$ . The larger  $p_4$ , the more bias its estimation acquires. For instance, in Fig. 4, the true value of  $p_4$  is 0.1 and the bias of the MLE is on the level of 10%,  $\langle X_{\text{est}} \rangle_{X=0.1} \simeq 0.11$ . To compensate for this bias, we calibrate the MLE by obtaining  $\langle X_{\text{est}} \rangle(X)$  from our MCTDH simulations, see [38]. Also,  $\partial \langle X_{\text{est}} \rangle_X / \partial X|_{X=0.1} \simeq 0.6$ , which then provides the mean-square deviation  $\langle (\delta X_{\text{est}})^2 \rangle_{X=0.1}$ . The inset in Fig. 4 verifies that, asymptotically,  $\langle (\delta X_{\text{est}})^2 \rangle_{X=0.1}$  approaches the Cramér-Rao lower bound for large  $\nu$ .

In conclusion, we have found, using a self-consistent many-body approach, that many-body metrology utilizing interacting trapped bosons needs to conform to the final self-consistently computed many-body state. The QFI completely depends on the parameter dependence of the final state itself, and is thus relatively unaffected by self-consistency (in the weakly interacting regime). However, even in the latter regime, the CFI for a parameter estimation experiment is strongly affected by self-consistency due to its sensitive dependence on the orbitals' time evolution. As a particularly notable example, fitting the outcome of a number-statistics experiment in a double well to conventional TMI gives a null result for estimating the slope parameter  $p_4$ . The SC approach we employ, however, enables  $p_4$  estimation. Metrology with trapped ultracold quantum gases thus in general requires self-consistency of dynamical evolution, to correctly predict the estimation precision that can be accomplished in a given metrological protocol.

This work has been supported by the National Research Foundation of Korea under Grants No. 2017R1A2A2A05001422 and No. 2020R1A2C2008103.

---

[1] C. W. Helstrom, Minimum mean-squared error of estimates in quantum statistics, *Physics Letters A* **25**, 101 (1967).  
 [2] C. W. Helstrom, Quantum detection and estimation theory, *Journal of Statistical Physics* **1**, 231 (1969).  
 [3] S. L. Braunstein and C. M. Caves, Statistical distance and the geometry of quantum states, *Phys. Rev. Lett.* **72**, 3439 (1994).  
 [4] S. L. Braunstein, C. M. Caves, and G. Milburn, Generalized Uncertainty Relations: Theory, Examples, and Lorentz Invariance, *Annals of Physics* **247**, 135 (1996).

[5] V. Giovannetti, S. Lloyd, and L. Maccone, Quantum Metrology, *Phys. Rev. Lett.* **96**, 010401 (2006).  
 [6] H. Wiseman and G. Milburn, *Quantum Measurement and Control* (Cambridge University Press, 2010).  
 [7] G. Tóth and I. Apellaniz, Quantum metrology from a quantum information science perspective, *Journal of Physics A: Mathematical and Theoretical* **47**, 424006 (2014).  
 [8] D. Braun, G. Adesso, F. Benatti, R. Floreanini, U. Marzolino, M. W. Mitchell, and S. Pirandola, Quantum-enhanced measurements without entanglement, *Rev. Mod. Phys.* **90**, 035006 (2018).  
 [9] R. Schnabel, N. Mavalvala, D. E. McClelland, and P. K. Lam, Quantum metrology for gravitational wave astronomy, *Nature Communications* **1**, 121 (2010).  
 [10] D. Braun, F. Scheiner, and U. R. Fischer, Intrinsic measurement errors for the speed of light in vacuum, *Classical and Quantum Gravity* **34**, 175009 (2017).  
 [11] V. Giovannetti, S. Lloyd, and L. Maccone, Advances in quantum metrology, *Nature Photonics* **5**, 222 (2011).  
 [12] S. Pirandola, B. R. Bardhan, T. Gehring, C. Weedbrook, and S. Lloyd, Advances in photonic quantum sensing, *Nature Photonics* **12**, 724 (2018).  
 [13] E. Polino, M. Valeri, N. Spagnolo, and F. Sciarrino, Photonic quantum metrology, *AVS Quantum Science* **2**, 024703 (2020).  
 [14] M. Barbieri, Optical Quantum Metrology, *PRX Quantum* **3**, 010202 (2022).  
 [15] L. Pezzè, L. A. Collins, A. Smerzi, G. P. Berman, and A. R. Bishop, Sub-shot-noise phase sensitivity with a Bose-Einstein condensate Mach-Zehnder interferometer, *Phys. Rev. A* **72**, 043612 (2005).  
 [16] S. Choi and B. Sundaram, Bose-Einstein condensate as a nonlinear Ramsey interferometer operating beyond the Heisenberg limit, *Phys. Rev. A* **77**, 053613 (2008).  
 [17] C. Gross, T. Zibold, E. Nicklas, J. Estève, and M. K. Oberthaler, Nonlinear atom interferometer surpasses classical precision limit, *Nature* **464**, 1165 (2010).  
 [18] J. Chwedeńczuk, F. Piazza, and A. Smerzi, Phase estimation with interfering Bose-Einstein-condensed atomic clouds, *Phys. Rev. A* **82**, 051601 (2010).  
 [19] J. Javanainen and H. Chen, Optimal measurement precision of a nonlinear interferometer, *Phys. Rev. A* **85**, 063605 (2012).  
 [20] C. Gross, Spin squeezing, entanglement and quantum metrology with Bose-Einstein condensates, *Journal of Physics B: Atomic, Molecular and Optical Physics* **45**, 103001 (2012).  
 [21] T. Berrada, S. van Frank, R. Bücker, T. Schumm, J. F. Schaff, and J. Schmiedmayer, Integrated Mach-Zehnder interferometer for Bose-Einstein condensates, *Nature Communications* **4**, 2077 (2013).  
 [22] W. Muessel, H. Strobel, D. Linnemann, D. B. Hume, and M. K. Oberthaler, Scalable Spin Squeezing for Quantum-Enhanced Magnetometry with Bose-Einstein Condensates, *Phys. Rev. Lett.* **113**, 103004 (2014).  
 [23] H. Strobel, W. Muessel, D. Linnemann, T. Zibold, D. B. Hume, L. Pezzè, A. Smerzi, and M. K. Oberthaler, Fisher information and entanglement of non-Gaussian spin states, *Science* **345**, 424 (2014).  
 [24] K. Gietka and J. Chwedeńczuk, Atom interferometer in a double-well potential, *Phys. Rev. A* **90**, 063601 (2014).  
 [25] J. Huang, S. Wu, H. Zhong, and C. Lee, Quantum metrology with cold atoms, in *Annual Review of Cold Atoms and Molecules* (2014)

- Chap. 7, pp. 365–415.
- [26] S. Ragole and J. M. Taylor, Interacting Atomic Interferometry for Rotation Sensing Approaching the Heisenberg Limit, *Phys. Rev. Lett.* **117**, 203002 (2016).
- [27] C. Luo, J. Huang, X. Zhang, and C. Lee, Heisenberg-limited Sagnac interferometer with multiparticle states, *Phys. Rev. A* **95**, 023608 (2017).
- [28] L. Pezzè, A. Smerzi, M. K. Oberthaler, R. Schmied, and P. Treutlein, Quantum metrology with nonclassical states of atomic ensembles, *Rev. Mod. Phys.* **90**, 035005 (2018), and the extensive list of references therein.
- [29] J. Czajkowski, K. Pawłowski, and R. Demkowicz-Dobrzański, Many-body effects in quantum metrology, *New Journal of Physics* **21**, 053031 (2019).
- [30] S. S. Szigeti, S. P. Nolan, J. D. Close, and S. A. Haine, High-Precision Quantum-Enhanced Gravimetry with a Bose-Einstein Condensate, *Phys. Rev. Lett.* **125**, 100402 (2020).
- [31] S. Boixo, S. T. Flammia, C. M. Caves, and J. M. Geremia, Generalized Limits for Single-Parameter Quantum Estimation, *Phys. Rev. Lett.* **98**, 090401 (2007).
- [32] S. Boixo, A. Datta, S. T. Flammia, A. Shaji, E. Bagan, and C. M. Caves, Quantum-limited metrology with product states, *Phys. Rev. A* **77**, 012317 (2008).
- [33] A. I. Streltsov, O. E. Alon, and L. S. Cederbaum, General variational many-body theory with complete self-consistency for trapped bosonic systems, *Phys. Rev. A* **73**, 063626 (2006).
- [34] O. E. Alon, A. I. Streltsov, and L. S. Cederbaum, Multiconfigurational time-dependent Hartree method for bosons: Many-body dynamics of bosonic systems, *Phys. Rev. A* **77**, 033613 (2008).
- [35] A. U. J. Lode, C. Lévêque, L. B. Madsen, A. I. Streltsov, and O. E. Alon, Colloquium: Multiconfigurational time-dependent Hartree approaches for indistinguishable particles, *Rev. Mod. Phys.* **92**, 011001 (2020).
- [36] R. Lin, P. Mognini, L. Papariello, M. C. Tsatsos, C. Lévêque, S. E. Weiner, E. Fasshauer, R. Chitra, and A. U. J. Lode, MCTDH-X: The multiconfigurational time-dependent Hartree method for indistinguishable particles software, *Quantum Science and Technology* **5**, 024004 (2020).
- [37] O. E. Alon and L. S. Cederbaum, Pathway from Condensation via Fragmentation to Fermionization of Cold Bosonic Systems, *Phys. Rev. Lett.* **95**, 140402 (2005).
- [38] The Supplemental Material, which quotes Refs. [55–57], contains a description of the MCTDH method and derivations of metrological quantities within the MCTDH framework, such as quantum Fisher information, probability distribution (likelihood), and details on the maximum likelihood estimator, as well as convergence studies for  $M > 2$ . Equation numbers quoted in the main text in the format (S#) refer to equations in the supplement.
- [39] Details on the MCTDH-X implementation of MCTDH, used to solve Eqs. (S1) in [38], can be found in Ref. [36].
- [40] A. Fujiwara and H. Nagaoka, Quantum Fisher metric and estimation for pure state models, *Physics Letters A* **201**, 119 (1995).
- [41] O. E. Barndorff-Nielsen and R. D. Gill, Fisher information in quantum statistics, *Journal of Physics A: Mathematical and General* **33**, 4481 (2000).
- [42] S. Boixo, A. Datta, M. J. Davis, A. Shaji, A. B. Tacla, and C. M. Caves, Quantum-limited metrology and Bose-Einstein condensates, *Phys. Rev. A* **80**, 032103 (2009).
- [43] S. Alipour, M. Mehboudi, and A. T. Rezakhani, Quantum Metrology in Open Systems: Dissipative Cramér-Rao Bound, *Phys. Rev. Lett.* **112**, 120405 (2014).
- [44] T. Wasak, A. Smerzi, L. Pezzè, and J. Chwedeńczuk, Optimal measurements in phase estimation: simple examples, *Quantum Information Processing* **15**, 2231 (2016).
- [45] In  $^{87}\text{Rb}$ ,  $L = 1 \mu\text{m}$  yields a time unit  $\Delta t = 1.366$  msec.
- [46] M. Olshaniĭ, Atomic Scattering in the Presence of an External Confinement and a Gas of Impenetrable Bosons, *Phys. Rev. Lett.* **81**, 938 (1998).
- [47] J.-G. Baak and U. R. Fischer, Classical and quantum metrology of the Lieb-Liniger model, *Phys. Rev. A* **106**, 062442 (2022).
- [48] G. J. Milburn, J. Corney, E. M. Wright, and D. F. Walls, Quantum dynamics of an atomic Bose-Einstein condensate in a double-well potential, *Phys. Rev. A* **55**, 4318 (1997).
- [49] E. H. Lieb and R. Seiringer, Proof of Bose-Einstein Condensation for Dilute Trapped Gases, *Phys. Rev. Lett.* **88**, 170409 (2002).
- [50] E. H. Lieb, R. Seiringer, and J. Yngvason, One-Dimensional Bosons in Three-Dimensional Traps, *Phys. Rev. Lett.* **91**, 150401 (2003).
- [51] O. Penrose and L. Onsager, Bose-Einstein Condensation and Liquid Helium, *Phys. Rev.* **104**, 576 (1956).
- [52] This may be explained by the fact that terms containing Fock space coefficients only and those involving orbitals in  $\mathfrak{F}^X$  (Eq. (S4) in [38]) tend to compensate each other.
- [53] R. A. Fisher, On the mathematical foundations of theoretical statistics, *Philosophical Transactions of the Royal Society of London A* **222**, 309 (1922).
- [54] R. A. Fisher, Theory of Statistical Estimation, *Mathematical Proceedings of the Cambridge Philosophical Society* **22**, 309 (1922).
- [55] R. Rossi, *Mathematical Statistics: An Introduction to Likelihood Based Inference* (Wiley, 2018).
- [56] K.-S. Lee and U. R. Fischer, Truncated many-body dynamics of interacting bosons: A variational principle with error monitoring, *International Journal of Modern Physics B* **28**, 1550021 (2014).
- [57] A. Nijenhuis and H. Wilf, *Combinatorial Algorithms: For Computers and Calculators*, edited by W. Rheinboldt, Computer science and applied mathematics (Elsevier Science, 2014).
- [58] X. Niu, S. Su, and J. Zheng, A New Fast Computation of a Permanent, *IOP Conference Series: Materials Science and Engineering* **790**, 012001 (2020).

## SUPPLEMENTAL MATERIAL

### I. Multiconfigurational time-dependent Hartree theory

Given a set of coefficients and a set of orbitals for an initial state, the time evolution in the MCTDH framework proceeds according to the following system of equations:

$$\begin{aligned} i \frac{\partial \mathbf{C}(t)}{\partial t} &= \mathbf{H}(t) \mathbf{C}(t), \\ i \partial_t |\phi_j\rangle &= \hat{P} \left[ \hat{h} |\phi_j\rangle + \sum_{k,s,q,l} [\rho^{-1}]_{jk} \rho_{ksql} \hat{W}_{sl} |\phi_q\rangle \right], \end{aligned} \quad (\text{S1})$$

which is derived by applying the time-dependent variational principle to the interacting  $N$ -body Hamiltonian  $\hat{H} = \sum_{j=1}^N \hat{h}(x_j) + \sum_{j<k} \hat{W}(x_j - x_k)$  [34]. Here,  $\mathbf{C}(t)$  is a column vector that consists of all possible expansion coefficients  $C_{\bar{n}}(t)$  and  $\mathbf{H}(t)$  corresponds to the time-dependent Hamiltonian matrix in the basis  $\{|\bar{n}(t)\rangle\}$ . Also,  $\hat{h}$  is a single-particle Hamiltonian,  $\hat{W}_{sl} = \int dx' \phi_s^*(x') \hat{W}(x - x') \phi_l(x')$ , and  $\hat{P} = 1 - \sum_{j=1}^M |\phi_j\rangle \langle \phi_j|$  is an projection operator to the subspace that is orthogonal to the one spanned by orbitals. The  $[\rho^{-1}]_{jk}$  is a matrix element of the inverse of reduced one-body density matrix:

$$\begin{aligned} \rho(x, x'; t) &= \langle \Psi(t) | \hat{\Psi}^\dagger(x') \hat{\Psi}(x) | \Psi(t) \rangle \\ &= \sum_{k,q} \phi_k^*(x', t) \phi_q(x, t) \langle \Psi(t) | \hat{b}_k^\dagger(t) \hat{b}_q(t) | \Psi(t) \rangle \\ &= \sum_{k,q} \phi_k^*(x', t) \phi_q(x, t) \rho_{kq}(t), \end{aligned} \quad (\text{S2})$$

where the  $\rho_{kq}$  is, for the cases of  $k = q$  and  $k \neq q$ ,

$$\rho_{kk} = \sum_{\bar{n}} |C_{\bar{n}}(t)|^2 n_k, \quad \rho_{kq} = \sum_{\bar{n}} C_{\bar{n}}^*(t) C_{\bar{n}_k^q}(t) \sqrt{n_k(n_q + 1)}.$$

Similarly,  $\rho_{ksql}$  is a matrix element of the reduced two-body matrix

$$\begin{aligned} \rho(x_1, x_2, x'_1, x'_2; t) &= \langle \Psi(t) | \hat{\Psi}^\dagger(x'_1) \hat{\Psi}^\dagger(x'_2) \hat{\Psi}(x_1) \hat{\Psi}(x_2) | \Psi(t) \rangle \\ &= \sum_{k,s,q,l} \phi_k^*(x'_1, t) \phi_s^*(x'_2, t) \phi_q(x_1, t) \phi_l(x_2, t) \rho_{ksql}(t), \end{aligned} \quad (\text{S3})$$

where

$$\begin{aligned} \rho_{kkkk} &= \sum_{\bar{n}} |C_{\bar{n}}(t)|^2 n_k(n_k - 1), \quad \rho_{kssk} = \sum_{\bar{n}} |C_{\bar{n}}(t)|^2 n_k n_s, \\ \rho_{kkqq} &= \sum_{\bar{n}} C_{\bar{n}}^*(t) C_{\bar{n}_{kk}^{qq}}(t) \sqrt{(n_k - 1)n_k(n_q + 1)(n_q + 2)}, \quad \rho_{kkkl} = \sum_{\bar{n}} C_{\bar{n}}^*(t) C_{\bar{n}_k^l}(t) (n_k - 1) \sqrt{n_k(n_l + 1)}, \\ \rho_{ksss} &= \sum_{\bar{n}} C_{\bar{n}}^*(t) C_{\bar{n}_k^s}(t) n_s \sqrt{n_k(n_s + 1)}, \quad \rho_{kkql} = \sum_{\bar{n}} C_{\bar{n}}^*(t) C_{\bar{n}_{kk}^{ql}}(t) \sqrt{(n_k - 1)n_k(n_q + 1)(n_l + 1)}, \\ \rho_{ksqq} &= \sum_{\bar{n}} C_{\bar{n}}^*(t) C_{\bar{n}_{ks}^{qq}}(t) \sqrt{n_k n_s (n_q + 1)(n_q + 2)}, \quad \rho_{kssl} = \sum_{\bar{n}} C_{\bar{n}}^*(t) C_{\bar{n}_k^l}(t) n_s \sqrt{n_k(n_l + 1)}, \\ \rho_{ksql} &= \sum_{\bar{n}} C_{\bar{n}}^*(t) C_{\bar{n}_{ks}^{ql}}(t) \sqrt{n_k n_s (n_q + 1)(n_l + 1)}. \end{aligned}$$

Infinite resources for numerical calculation makes it possible to assume the theoretical limit  $M \rightarrow \infty$ , thus  $\hat{P} \rightarrow \hat{0}$  and  $\partial_t |\phi_j\rangle = 0$  in Eq. (S1), which means that a complete set of time-independent orbitals  $\{\phi_j(x) | j = 1, 2, \dots\}$  can be composed and the dynamics of systems is fully described only by the set of coefficients  $\{C_{\bar{n}}(t)\}$ , from which all quantum metrological properties can be extracted.

If  $M = 2$ , with fixed orbitals, is adequate for the description of a system, the modes comprise the conventional TMI, using a  $SU(2)$  formulation. Optical systems have been used to realize such two-mode systems, e.g., a Mach-Zehnder interferometer, where only the Fock space coefficients matter to predict the number of photons in each interferometric arm. However, for interacting atoms, an exact description requires infinite  $M$ , and truncating at finite  $M$  is valid only approximately, cf. the error-controlled extension of multiconfigurational Hartree put forth in [56]. As the interaction becomes weaker, a description in terms of finite  $M$  improves. The self-consistent MCTDH framework here goes significantly further than a conventional TMI and introduces time-evolving orbitals of changing shape. We also note here that a Hartree-Fock method, using plane waves for the field operator expansion as appropriate in a translationally invariant system, will fail to capture a trapped system when, as necessary for finite computational resources, the expansion is truncated at a finite  $M$ .

## II. Quantum Fisher information of a pure state in the MCTDH framework

Because of the introduction of time-evolving orbitals, a formulation of the QFI is required which facilitates incorporating the result of solving the MCTDH time evolution in Eqs. (S1). The QFI, which is the ultimate limit of precision given by  $|\psi_X\rangle$ , is calculated by  $\mathfrak{F}_X = 4(\langle\partial_X\psi_X|\partial_X\psi_X\rangle - |\langle\psi_X|\partial_X\psi_X\rangle|^2)$  for general pure states, and for some state represented as Eq. (1), we have, for any number of modes,

$$\begin{aligned} \mathfrak{F}_X/4 &= \sum_{\vec{n}} \partial_X C_{\vec{n}}^* \partial_X C_{\vec{n}} - \left| \sum_{\vec{n}} C_{\vec{n}}^* \partial_X C_{\vec{n}} \right|^2 \\ &+ \sum_{\vec{n}} \sum_{k,q} (\partial_X C_{\vec{n}}^* C_{\vec{n}_k^q} - C_{\vec{n}}^* \partial_X C_{\vec{n}_k^q}) (\partial_X)_{kq} \zeta_{qk} - \sum_{\vec{n}} (\partial_X C_{\vec{n}}^* C_{\vec{n}} - C_{\vec{n}}^* \partial_X C_{\vec{n}}) \sum_{k,q} (\partial_X)_{kq} \rho_{kq} \\ &- \sum_{k,s,q} (\partial_X)_{ks} (\partial_X)_{sq} \rho_{kq} + \left( \sum_{k,q} (\partial_X)_{kq} \rho_{kq} \right)^2 - \sum_{k,s,q,l} (\partial_X)_{kq} (\partial_X)_{sl} \rho_{ksql}, \end{aligned} \quad (\text{S4})$$

where  $\zeta_{qk} := \sqrt{n_k(n_q + 1)}$  or  $\zeta_{qk} := n_k$  if  $q \neq k$  or  $q = k$ , respectively, and  $(\partial_X)_{kq} := \int dx \phi_k^*(x,t) \partial_X \phi_q(x,t)$ . Refer to Eq. (S2) and Eq. (S3) for the definitions of  $\rho_{kq}$  and  $\rho_{ksql}$ . The first two terms involve only the coefficients and the remaining terms are related to the changes of coefficients and orbitals, for infinitesimal increment of  $X$ . In summary, Eq. (S4) completely incorporates the information orbitals as well as coefficients changing with  $X$ .

## III. Construction of the probability distribution (likelihood) in MCTDH for bosons

Here we explain how to construct the probability distribution of measurement outcomes. This process obviously depends on the specific systems and the choice of measurement. Here, the metrological implementation with the ultracold bosons trapped in a double-well potential is covered and the number of particles in each well is counted after the time evolution is finished, and considered as the measurement. The probability of a particle in  $\phi_j(x,t)$  to be found at the left ( $L$ ) or the right ( $R$ ) is defined as

$$P_{L,j} = \int_{-\infty}^0 |\phi_j(x,t)|^2 dx, \quad P_{R,j} = \int_0^{\infty} |\phi_j(x,t)|^2 dx, \quad (\text{S5})$$

where we assume that the center of the 1D potential is at  $x = 0$ .

Next, we need to consider the combinatorial problem related to many particles and bosonic statistics. Let us take for simplicity the example of  $N = 2$ . There are three measurement outcomes:  $\vec{n} := (n_L, n_R) = (2, 0)$ ,  $(1, 1)$ , and  $(0, 2)$ , in which  $n_L$  and  $n_R$  mean the numbers of particles found in the left well and in the right well, respectively. When the final state is  $\sum_{\vec{n}} C_{\vec{n}} |\vec{n}\rangle = \sum_{k=0}^2 C_k |2-k, k\rangle$ , the probability for each case is as follows:

$$\begin{aligned} P_0 &= P(\vec{n} = (2, 0)) = |C_0|^2 P_{L,1}^2 + |C_1|^2 P_{L,1} P_{L,2} + |C_2|^2 P_{L,2}^2, \\ P_1 &= P(\vec{n} = (1, 1)) = 2 |C_0|^2 P_{L,1} P_{R,1} + |C_1|^2 (P_{L,1} P_{R,2} + P_{R,1} P_{L,2}) + 2 |C_2|^2 P_{L,2} P_{R,2}, \\ P_2 &= P(\vec{n} = (0, 2)) = |C_0|^2 P_{R,1}^2 + |C_1|^2 P_{R,1} P_{R,2} + |C_2|^2 P_{R,2}^2, \end{aligned} \quad (\text{S6})$$

where it is trivial to show that  $P(\vec{n} = (2, 0)) + P(\vec{n} = (1, 1)) + P(\vec{n} = (0, 2)) = 1$  using  $P_{j,L} + P_{j,R} = 1$  and



$|C_0|^2 + |C_1|^2 + |C_2|^2 = 1$ . After careful inspection, one can rewrite the above probabilities as

$$\begin{aligned} P_0 &= P(\vec{\mathbf{n}} = (2, 0)) = \frac{|C_0|^2}{2} \begin{Bmatrix} P_{L,1} & P_{L,1} \\ P_{L,1} & P_{L,1} \end{Bmatrix} + \frac{|C_1|^2}{2} \begin{Bmatrix} P_{L,1} & P_{L,2} \\ P_{L,1} & P_{L,2} \end{Bmatrix} + \frac{|C_2|^2}{2} \begin{Bmatrix} P_{L,2} & P_{L,2} \\ P_{L,2} & P_{L,2} \end{Bmatrix}, \\ P_1 &= P(\vec{\mathbf{n}} = (1, 1)) = |C_0|^2 \begin{Bmatrix} P_{L,1} & P_{L,1} \\ P_{R,1} & P_{R,1} \end{Bmatrix} + |C_1|^2 \begin{Bmatrix} P_{L,1} & P_{L,2} \\ P_{R,1} & P_{R,2} \end{Bmatrix} + |C_2|^2 \begin{Bmatrix} P_{L,2} & P_{L,2} \\ P_{R,2} & P_{R,2} \end{Bmatrix}, \\ P_2 &= P(\vec{\mathbf{n}} = (0, 2)) = \frac{|C_0|^2}{2} \begin{Bmatrix} P_{R,1} & P_{R,1} \\ P_{R,1} & P_{R,1} \end{Bmatrix} + \frac{|C_1|^2}{2} \begin{Bmatrix} P_{R,1} & P_{R,2} \\ P_{R,1} & P_{R,2} \end{Bmatrix} + \frac{|C_2|^2}{2} \begin{Bmatrix} P_{R,2} & P_{R,2} \\ P_{R,2} & P_{R,2} \end{Bmatrix}, \end{aligned} \quad (\text{S7})$$

in which  $\{V\}$  means the permanent of a matrix  $V$ . By tracing the factor in front of each term and by considering bosonic statistics, one can find a regular pattern and generalize as follows:

$$P_j = P(\vec{\mathbf{n}} = (N - j, j)) = \frac{1}{N!} \binom{N}{j} \sum_{k=0}^N |C_k|^2 \{V_{j,k}\}, \quad (\text{S8})$$

where  $V_{j,k}$  is a special  $N \times N$  matrix, defined as below. The  $j$  is the number of particles in the right well, i.e.  $\vec{\mathbf{n}} = (N - j, j)$  and the  $k$  means  $\vec{\mathbf{n}} = (N - k, k)$ . The example above shows how to compose the matrix  $V_{j,k}$ . In order to compose  $V_{1,2}$ , for example, “1” is represented as  $\{L, R\}$  and the “2” is represented as  $\{2, 2\}$ . The former is an ordered set of  $N - j$  of  $L$  and  $j$  of  $R$ , and the latter is a conversion of “how many particles there are in each mode” into an (ascending-)ordered set of the occupied mode numbers:

$$\begin{aligned} j = 0 : (2, 0) &\rightarrow \{L, L\}, & j = 1 : (1, 1) &\rightarrow \{L, R\}, & j = 2 : (0, 2) &\rightarrow \{R, R\}, \\ k = 0 : (2, 0) &\rightarrow \{1, 1\}, & k = 1 : (1, 1) &\rightarrow \{1, 2\}, & k = 2 : (0, 2) &\rightarrow \{2, 2\}. \end{aligned}$$

Then the former set makes up the row indices and the latter set makes up the column indices:

$$\begin{array}{c} 2 \ 2 \\ L \\ R \end{array} \rightarrow \begin{pmatrix} P_{L,2} & P_{L,2} \\ P_{R,2} & P_{R,2} \end{pmatrix} = V_{1,2}, \quad (\text{S9})$$

and its permanent is now readily obtained to be

$$\{V_{1,2}\} = \begin{Bmatrix} P_{L,2} & P_{L,2} \\ P_{R,2} & P_{R,2} \end{Bmatrix} = P_{L,2} P_{R,2} + P_{L,2} P_{R,2}. \quad (\text{S10})$$

For another example, let us suppose that  $N = 3$  and try to express  $V_{1,2}$ . The first subscript 1 is converted into  $\{L, L, R\}$  and the second one 2 is converted into  $\{1, 2, 2\}$ . Then

$$\begin{array}{c} 1 \ 2 \ 2 \\ L \\ L \\ R \end{array} \rightarrow \begin{pmatrix} P_{L,1} & P_{L,2} & P_{L,2} \\ P_{L,1} & P_{L,2} & P_{L,2} \\ P_{R,1} & P_{R,2} & P_{R,2} \end{pmatrix} = V_{1,2}, \quad (\text{S11})$$

and the permanent is  $\{V_{1,2}\} = 4P_{L,1}P_{L,2}P_{R,2} + 2P_{L,2}^2P_{R,1}$ . Now we have all ingredients to construct the probability distribution of a measurement for which the number of particles in each well is counted. To calculate the permanent of a matrix, we used the advanced algorithm developed to reduce the algorithmic complexity in [57]; for an introduction see [58].

#### IV. Additional details on the MLE

##### *Construction of estimator and likelihood function*

The maximum likelihood estimator (abbreviated already in the main text as MLE) is a commonly used estimator in the field of statistics and is defined as follows:

$$X_{\text{est}} = \operatorname{argmax}_X P(\vec{\mathbf{n}}|X), \quad (\text{S12})$$

where  $\vec{n}$  is used to denote the measurement outcome. Also,  $\text{argmax}_X$  denotes, by definition of the MLE, the unique point in the domain of interest, at which the function values are maximized. Whenever an outcome  $\vec{n}$  is attained, one inserts it into the RHS of Eq. (S12) and finds a value of  $X$  that maximizes  $P(\vec{n}|X)$ . This is a one-shot estimate of  $X$ , namely  $X_{\text{est}}$ . In order to implement the MLE, it is necessary to obtain the likelihood function, i.e.,  $P(\vec{n}|X)$ , the process of which we now describe.

In the conventional TMI, only considering the change of Fock space coefficients,  $P(\vec{n}|X)$  is calculated as  $P(\vec{n}|X) = \langle \vec{n} | \hat{\Psi}(t) \rangle = |C_{\vec{n}}(t)|^2$ , where  $|\Psi(t)\rangle = \sum_{\vec{n}} C_{\vec{n}}(t) |\vec{n}\rangle$ . For the two-mode (double-well) system covered in the main text, cf. Eq. (3), we may consider the general two-mode state  $|\Psi(t)\rangle = \sum_{k=0}^N C_k(t) |N-k, k\rangle$ . Then  $\vec{n} = (n_1, n_2)$ , denoting that  $n_1$  particles are in  $\phi_1(x, t)$  and  $n_2$  particles in  $\phi_2(x, t)$ , is identified as the measurement result that  $n_1$  particles are in the left well and  $n_2$  particles are in the right well:  $\vec{n} = (n_L = n_1, n_R = n_2)$ . In particular, with the metrological protocol adopted in the main text, i.e.,  $|\Psi(t)\rangle = e^{-i(\epsilon \hat{J}_z + U \hat{J}_z^2)t} |\Psi(0)\rangle$ , each  $C_k(t)$  changes only by a phase (but not by magnitude):  $C_k(t) = \exp(-i\epsilon \frac{N-2k}{2} t) \exp(-iU(\frac{N-2k}{2})^2 t) C_k(0)$ , where  $\epsilon$  contains the information of  $X$ . Hence the likelihood  $P(\vec{n}|X)$  is independent of  $X$  and invariant, which leads to vanishing CFI, see also the constant orange dashed line (coh TMI) in Fig. 4.

In the self-consistent approach, however, the calculation of  $P(\vec{n}|X)$  depends on the specifics of each system and measurement considered, since the measurement results are affected by the changing orbitals as well as by the changing Fock space coefficients. A quantum state is now written as  $|\Psi(t)\rangle = \sum_{\vec{n}} C_{\vec{n}}(t) |\vec{n}(t)\rangle$ , indicating that the orbitals associated by the Fock space basis state  $|\vec{n}(t)\rangle$  evolve in time. In our double-well system, now  $\vec{n} = (n_1, n_2)$  cannot be interpreted as “ $n_1$  particles in the left well and  $n_2$  particles in the right well” anymore. The correct statement now is “ $n_1$  particles are in  $\phi_1(x, t)$  and  $n_2$  particles are in  $\phi_1(x, t)$ ”. The orbitals may delocalize as time passes, thus at the instant of measurement a particle in the orbital  $\phi_1(x, t)$  can be found in the left well or in the right well with some probabilities  $P_{L,1}$  or  $P_{R,1}$ , respectively, where  $P_{L,j} := \int_{-\infty}^0 |\phi_j(x, t)|^2 dx$  and  $P_{R,j} := \int_0^{\infty} |\phi_j(x, t)|^2 dx$ . In other words, at time  $t$ , it is necessary to take further probability distributions into account other than just  $|C_k(t)|^2$ :

$$P(\vec{n} = (N-j, j)|X) = |C_k(t)|^2, \quad \text{Conventional Two-Mode Interferometry} \quad (\text{S13})$$

$$P(\vec{n} = (N-j, j)|X) = \sum_{k=0} P_{j,k} |C_k(t)|^2, \quad \text{Self-Consistent Approach} \quad (\text{S14})$$

where the probability coefficients in (S14) read

$$P_{j,k} := \frac{1}{N!} \binom{N}{j} \{V_{j,k}\}.$$

We refer to Eq. (S8) and the discussion it follows for the definition and calculation of the special matrix  $\{V_{j,k}\}$ . In summary, the difference in obtaining the probabilities  $P(\vec{n}|X)$  as outlined in the above leads to a discrepancy in the probability distribution (synonymously likelihood), and therefore in the CFI and the MLE.

For further illustration of the importance of self-consistency, see Fig. S1. These plots show how the probability distribution, calculated by Eq. (S8), changes according to the double-well metrological scenario of the main text.

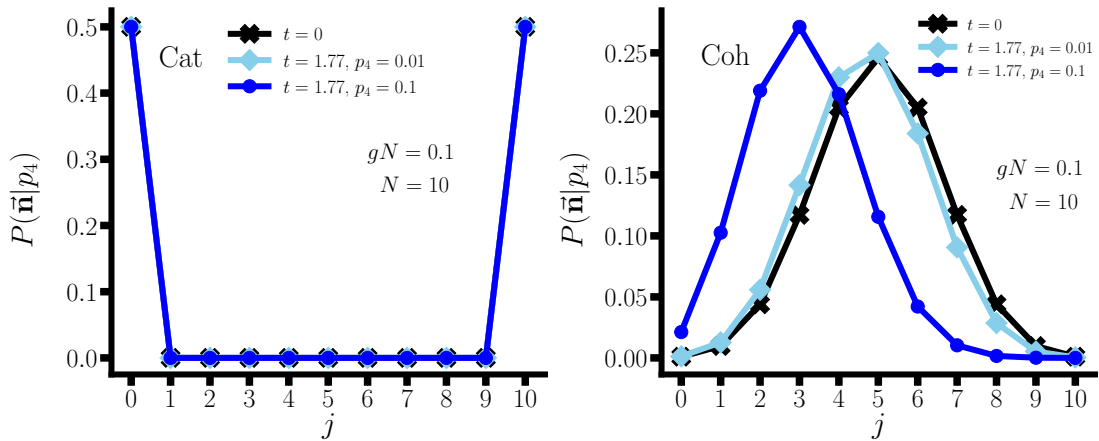


FIG. S1. Probability distributions for the measurement outcome  $\mathbf{n} = (n_L, n_R) = (N-j, j)$  with self-consistency taken into account.

For the cat state (left), delocalization of orbitals is weak, and the probability distribution almost does not change even within the self-consistent framework. Then self-consistent metrology simply repeats the results of conventional two-mode interferometry. However, in the case of a spin-coherent state (right), the probability distribution evolves in time because of delocalizing orbitals. The conventional two-mode interferometry, i.e., Eq. (S13), predicts that the probability distribution remains identical to the initial one at  $t = 0$  (black crosses). On the other hand, self-consistent metrology, i.e., Eq. (S14), predicts that the likelihood gets biased towards the left, and this is accurate since the particles are mostly located at the left well when  $p_4 > 0$ . As  $p_4$  increases, the likelihood gets even more biased, and this dependence on  $p_4$  results in a nonvanishing CFI.

*Further results on MLE statistics*

Additional details on the MLE are supplied in Fig. S2. The top left shows the mean of the maximum likelihood estimator with respect to the final state that has evolved under the true value of  $p_4$ . To calculate the mean, the probability distribution first needs to be composed. One measurement outcome is used at a single time of estimation, i.e.,  $\nu = 1$ . When the true value of  $p_4$  is 0.1,  $\langle X_{\text{est}} \rangle_X \simeq 0.0926$ . The top right plot shows the mean of the maximum likelihood estimator versus  $\nu$  when  $p_4 = 0.1$ , which is the number of measurement outcomes for a single estimation of  $p_4$ . As  $\nu$  increases,  $\langle X_{\text{est}} \rangle_X$  converges at around 0.11, which implies a bias of MLE. The bottom left shows this bias of the MLE, where  $|\partial \langle X_{\text{est}} \rangle_X / \partial X| \simeq 1$  near  $p_4 \simeq 0$ , which however does not hold as  $p_4$  deviates more significantly from zero. Finally, the bottom right shows the ratio between the mean-square deviation and the Cramér-Rao lower bound (CRLB). This ratio decreases as  $\nu$  increases: The MLE is known to make the mean-square deviation  $\langle (\delta X_{\text{est}})^2 \rangle_X$  converge to the CRLB as  $\nu \rightarrow \infty$  according to the central limit theorem, which is thus confirmed.

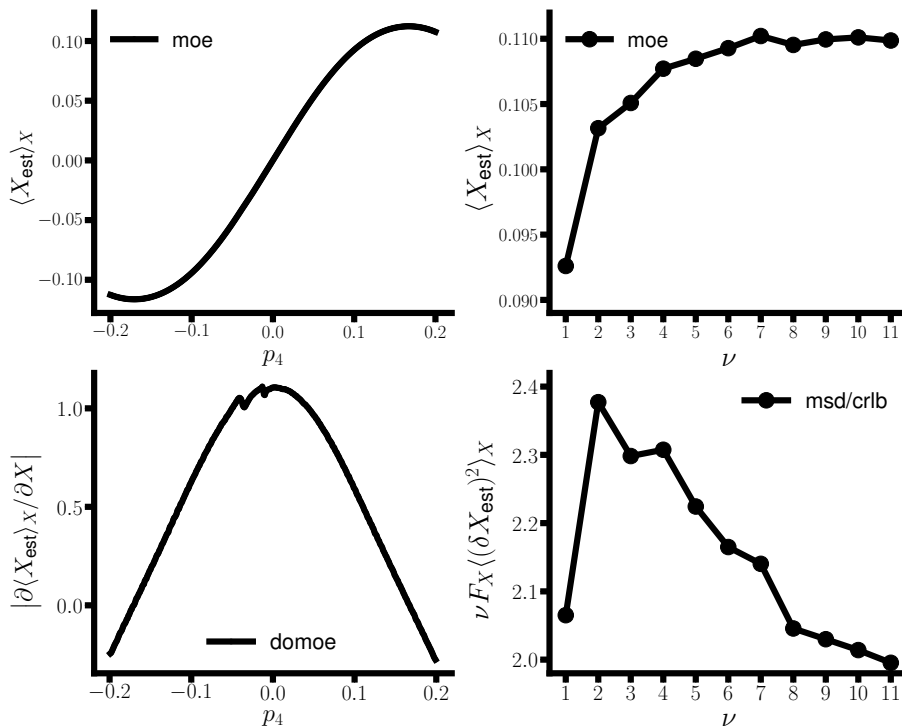


FIG. S2. Additional results on maximum likelihood estimation, where “moe” is the mean of estimates ( $\langle X_{\text{est}} \rangle_X$ ), “msd” is the mean-square deviation ( $\langle (\delta X_{\text{est}})^2 \rangle_X$ ), and “domoe” stands for the absolute value of the derivative of the mean of estimates ( $|\partial \langle X_{\text{est}} \rangle_X / \partial X|$ ).

### V. Convergence of results for increasing number of modes: $M = 2$ , $M = 3$ , and $M = 4$

In the main text, it is shown that even for a weakly interacting gas, studying the CFI can exhibit a discrepancy between two-mode interferometry and self-consistent metrology. By monitoring  $\rho_{\text{tm}}$ , the validity of the two-mode approximation,  $M = 2$ , had been confirmed in the time interval of interest, and accordingly, two modes are used in the self-consistent framework, too. In the weakly interacting regime, two modes explain the primary quantum dynamics of the system and thus, the quantum Fisher information which is governed by the final state can be predicted sufficiently accurate by two-mode metrology. Since interparticle interaction is weak, i.e.,  $gN = 0.1$ ,  $M = 2$  is thus used for the self-consistent results.

To verify the validity of the two-mode approximation, we compare here with the  $M = 3$  and  $M = 4$  cases in a similar regimes of parameters, namely,  $gN = 0.1$ ,  $N = 2$ , and  $t = 0 \sim 4$ . The validity of two-mode approximation is checked in Fig. S3. For  $M = 3$  and  $M = 4$ , it is evident that  $\rho_{\text{tm}} \lesssim 1$ , implying that the two-mode approximation works; the additional modes are rarely occupied during this time period. The impact of the additional modes is thus not crucial.

This also can be seen in the QFI with respect to the parameter  $p_4$ ; see upper row in Fig. S4. For the weakly interacting gas, a small number of modes, e.g. here  $M = 2$ , is sufficient to describe the dynamics of the system and thus non-self-consistent two-mode interferometry calculates the QFI rather precisely. The self-consistent results with two (yellow solid), three (orange dash-dotted), and four (red dotted) modes are almost identical, and are not significantly different from the value of two-mode interferometry (black solid).

We have seen in the main text that the CFI for  $p_4$  can significantly differ when evaluated in the non-self-consistent and self-consistent frameworks. The lower row in Fig. S4 shows that the inclusion of more orbitals reproduces (and thus also further emphasizes) the different predictions made for  $M = 2$  in the main text, when comparing the CFI in a self-consistent metrological framework relative to that in a non-self-consistent one. In the bottom left of Fig. S4, with a cat distribution of the coefficients of the initial state, the CFI for a certain measurement, i.e., measuring the number of particles in the left and right well, remains almost zero. On the other hand, in the bottom right of Fig. S4, with a spin-coherent distribution of the coefficients of the initial state, the CFI is nonvanishing as time passes by. This is confirmed for  $M = 2$  (yellow solid),  $M = 3$  (orange dash-dot), and  $M = 4$  (red dotted). The nonvanishing CFI *cannot* be predicted in the conventional framework of non-self-consistent two-mode interferometry. The self-consistent approach thus makes it possible at all to accurately evaluate the precision limit for estimating the parameter  $p_4$ .

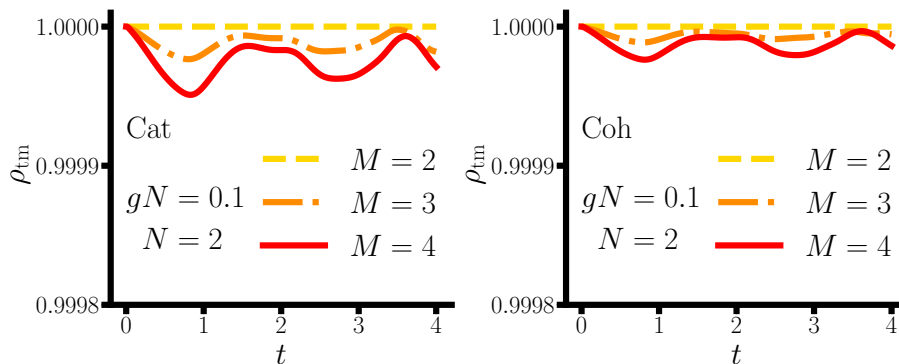


FIG. S3. Monitoring the two-mode truncation after  $p_4$  is turned on, by verifying whether  $\rho_{\text{tm}} = (\rho_1 + \rho_2)/N \lesssim 1$  (we put  $N = 10$ ), with  $gN$  values as indicated. Cat state is on the left and spin-coherent state on the right.

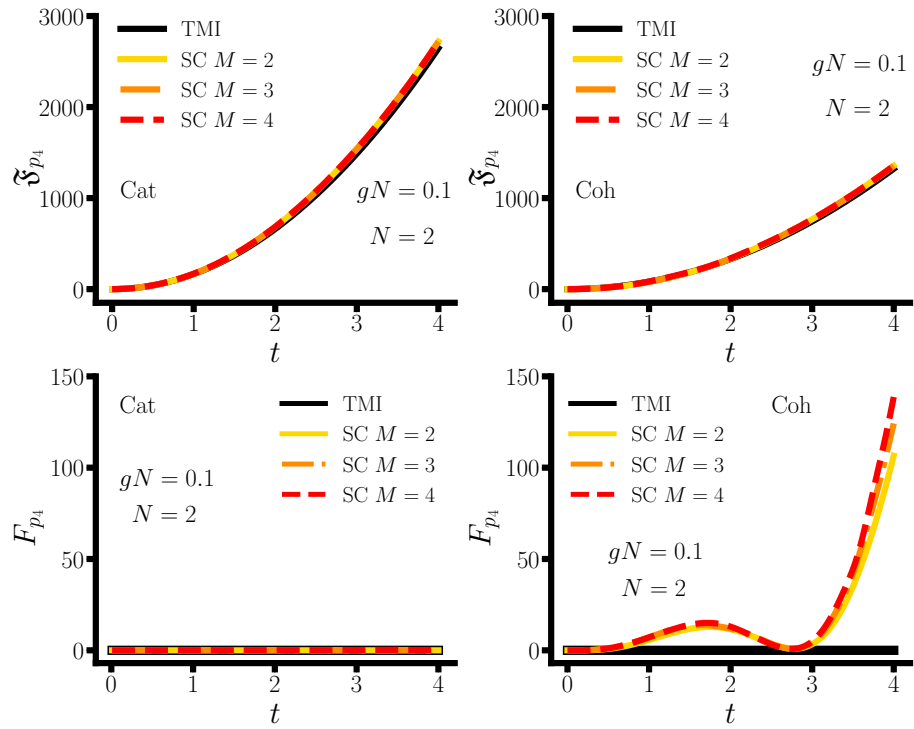


FIG. S4. First and second row display quantum ( $\mathfrak{F}$ ) and classical ( $F$ ) Fisher information, respectively, plotted versus time  $t$ , for cat and coherent (coh) states, respectively.